

Nanoscale

Accepted Manuscript



This is an *Accepted Manuscript*, which has been through the Royal Society of Chemistry peer review process and has been accepted for publication.

Accepted Manuscripts are published online shortly after acceptance, before technical editing, formatting and proof reading. Using this free service, authors can make their results available to the community, in citable form, before we publish the edited article. We will replace this *Accepted Manuscript* with the edited and formatted *Advance Article* as soon as it is available.

You can find more information about *Accepted Manuscripts* in the [Information for Authors](#).

Please note that technical editing may introduce minor changes to the text and/or graphics, which may alter content. The journal's standard [Terms & Conditions](#) and the [Ethical guidelines](#) still apply. In no event shall the Royal Society of Chemistry be held responsible for any errors or omissions in this *Accepted Manuscript* or any consequences arising from the use of any information it contains.

Targeting FR-expressing cells in ovarian cancer with Fab-functionalized nanoparticles: a full study to provide the proof of principle from *in vitro* to *in vivo*

Alessandra Quarta^{§*}, *Davide Bernareggi*^{†*}, *Fabio Benigni*[•], *Elena Luison*[‡], *Giuseppe Nano*[¶], *Simone Nitti*[†], *Maria Candida Cesta*[¶], *Luciano Di Ciccio*[¶], *Silvana Canevari*[‡], *Teresa Pellegrino*^{§†&} and *Mariangela Figini*^{‡§}

& Nanoscience Institute of CNR National Nanotechnology Laboratory Via Arnesano, I-73100 Lecce (Italy)

† Istituto Italiano di Tecnologia, Via Morego 30, I-16163 Genova (Italy),

‡ Fondazione IRCCS Istituto Nazionale dei Tumori Milano, DOSMM Molecular Therapies Unit, 20133 Milano (Italy)

• San Raffaele Scientific Institute, URI, Via Olgettina 60 20132 Milan, (Italy)

¶ Dompé S.p.A.. Via Campo di Pile, 67100 - L'Aquila (Italy)

§ corresponding authors: mariangela.figini@istitutotumori.mi.it and teresa.pellegrino@iit.it

*these authors have contributed equally to this work

KEYWORDS: *Ovarian cancer, magnetic nanoparticles, antibodies, in vivo targeting*

Abstract

Efficient targeting in tumor therapies is still an open issue: systemic biodistribution and poor specific accumulation of drugs weaken efficacy of treatments. Engineered nanoparticles are expected to bring benefits allowing specific delivery of drug to the tumor or acting themselves as localized therapeutic agents. In this study we have targeted epithelial ovarian cancer with inorganic nanoparticles conjugated to a human antibody fragment against the folate receptor over-expressed on cancer cells. The conjugation approach is generally applicable. Indeed several types of nanoparticles (either magnetic or fluorescent) were engineered with the fragment, and their biological activity was preserved as demonstrated by biochemical methods *in vitro*.

In vivo studies with mice bearing orthotopic and subcutaneous tumors were performed. Elemental and histological analysis showed that the conjugated magnetic nanoparticles accumulated specifically and were retained at tumor site longer than the non-conjugated nanoparticles.

Introduction

In recent years, different strategies for developing targeted cancer therapy have been attempted. Among various targeting agents, monoclonal antibodies have been used either as directly active therapeutic agents or exploited as carriers for the delivery of conventional drugs.¹ With regard to targeted anti-tumor therapy in ovarian cancer, some antibodies are already clinically approved and others are under clinical development.² Mesoscale carriers of few tens to few hundreds of nanometers, for encapsulating antitumor drugs and targeted with antitumor antibodies have been also reported.³ Most of them are polymeric nanoparticles⁴⁻⁶, micelles^{7,8}, or liposomes^{9,10}.

More recently, inorganic nanocrystals made of different materials have gained interest as drug delivery systems.¹¹ Their intrinsic physical features (optical or magnetic) due to the reduced size, combined to the high surface to volume ratio for better surface functionalization with molecules of the same size range, like peptides or monoclonal antibodies, have prompted the investigations to create innovative and advanced diagnostic and therapeutic tools.¹²⁻¹⁵ Superparamagnetic iron oxide nanoparticles are perhaps the most promising nanotools for clinical applications, due to their magnetic properties as well as the good biocompatibility and the known biodegradability *in vivo* through the iron metabolism route.^{13, 16-18} They are already used in clinics as contrast agents in magnetic resonance imaging (MRI)¹⁹⁻²¹ and they have been also approved as medical devices in Europe as heat mediators for the treatment of glioblastoma *via* hyperthermia.²²⁻²⁵

Several functionalization approaches have been developed with the goal to have nanocrystals more stable in physiological media, well tolerated by the immune system, armed with anticancer agents, and properly bio-targeted.²⁶⁻³¹

Indeed, an effective biomolecular targeting strategy would lead to enhanced accumulation to the tumor of nanoparticles and eventually drug molecules associated to them, hence ultimately reducing side effects and toxicity due to systemic distribution.

Several studies already addressed the *in vivo* tumor targeting of Magnetic NanoParticles (MNP), both by validating their diagnostic relevance as MRI probes and assessing their biodistribution and safety.³²⁻³⁸ In addition, targeting capabilities were implemented by using chemical coupling of either tumor-homing peptides,^{37, 39} or, more commonly, specific antitumor antibodies, to the nanocrystals surface.³²⁻³⁵ At the state of art, there is a lack of knowledge on specific antibodies targeting of MNPs to ovarian cancer.

Epithelial ovarian cancer (EOC) is the leading cause of death from gynecological malignancies due to late diagnosis and high frequency of relapse occurrence.⁴⁰ Current treatments rely on surgery combined with chemotherapy. Despite the initial response to the treatment, most patients relapse and develop chemoresistance.^{41, 42} Consequently, in order to improve dosage modulation and duration of the chemotherapy, and to obtain a more specific delivery of the anticancer agents at the target site, more effective treatments are urgently needed. Presently, only few examples of *in vivo* EOC targeting with MNP have been reported^{39, 43} in which small peptides were used to functionalize MNP for targeting and sorting ovarian cells from ascitic liquid.³⁹

In the present study, we have engineered the surface of iron oxide nanocrystals to allow stable coupling with an antibody fragment that targets the α -isoform of the Folate Receptor (α FR), which is typically over-expressed on the membrane of EOC cells. The Anti Folate Receptor Antibody (AFRA) is a human antibody Fab fragment generated by conversion of the murine anti α FR antibody (MOV19), through production of EOC patients-derived phage display antibody library and guided selection, as previously described.⁴⁴ Fully human antibody fragments obtained by protein engineering and the use of locoregional treatments for some malignancies, such as intraperitoneal

delivery in EOC patients, may certainly represent promising approaches for overcoming some of the limitations of current therapeutic tools, and among them mainly the poor tumor penetration.

The advantage of using a Fab fragment instead of an entire IgG mainly resides in the reduced size of the final nanostructure. Indeed, it has been recently reported that nanoparticles, when covalently coupled with antibody fragments, rather than with entire immunoglobulin, are internalized to an higher extent. This evidence is most likely explained by the smaller size of the resulting nanoparticle-antibody fragment complex and the resulting better stability of the conjugates in physiological conditions.³³

With the goal of evaluating the targeting capacity of inorganic nanoparticle-antibody conjugates, we extended the AFRA conjugation chemistry to different types of nanocrystals including fluorescent quantum rods or spherical magnetic iron oxide nanoparticles (MNP-AFRAs) at different sizes (10 and 20 nm respectively).

in vitro analysis, including cytofluorimetry, binding analysis under flow conditions towards the isolated recombinant α FR (Biacore®), electron microscopy, iron uptake, FACS analysis, viability assay was carried out with 10 and 20 nm size MNP (MNP10 and MNP20), in order to prove the direct targeting efficiency and discriminate their biocompatible behavior. Optimal *in vitro* stability and specificity features were a prerequisite to select only specific magnetic bioconjugates for *in vivo* studies in ovarian cancer models. Among all the produced and characterized functionalized-nanoparticles, both the 10 and 20 nm MNP have satisfied the binding and colloidal stability performance requested for further *in vivo* characterization. To evaluate biodistribution, tumor accumulation and clearance following systemic or local administration route and at the same time minimize the number of animal used in this study, we have chosen however only one bio-conjugate based on the 20 nm MNPs (MNP20-AFRA and the corresponding pegylated sample named MNP20-PEG) as indeed this nanoparticle size matches also the ideal size range for iron oxide to achieve the highest heat performance in hyperthermia.

The overall results achieved here show the complexity and the challenges posed by targeted bio-inorganic systems preparations but also the great potential of MNPs-AFRA as novel tumor targeting tools with enhanced tumor accumulation performance. Additional work is clearly required to fully understand the therapeutic potential of such bioconjugates and their use for enhanced drug delivery or MNP-mediated hyperthermia applications in the treatment of ovarian cancer.

Results and Discussion

Preparation and structural characterization of the NP-AFRA conjugates

Conjugation of AFRA to inorganic nanoparticles was carried out according to the conjugation steps schematically depicted in Figure 1. In the first step, the nanoparticles were transferred from organic to water phase by amphiphilic polymer wrapping, following a previously reported protocol.^{45, 46} Di-amino polyethylene glycol (PEG) molecules were then covalently linked to the outer carboxylic groups of the polymer shell via EDC chemistry. The addition of PEG has the dual function to increase the stability of the nanoparticles^{47, 48}, and to introduce free amino groups available for next binding step.⁴⁹ Prior to conjugation to the nanoparticles, AFRA was provided as a glutathione-protected complex and it was first activated through reduction of the S-S bond. The cross-linker sulfo-SMCC was initially bound, *via* its *N*-hydroxyl succinimido (NHS) group, to the free amino

moiety of amino-PEG-derivatized nanoparticles; finally, the maleimido group was coupled with the free thiol group of the reduced AFRA to form a covalent thio-ether bond.

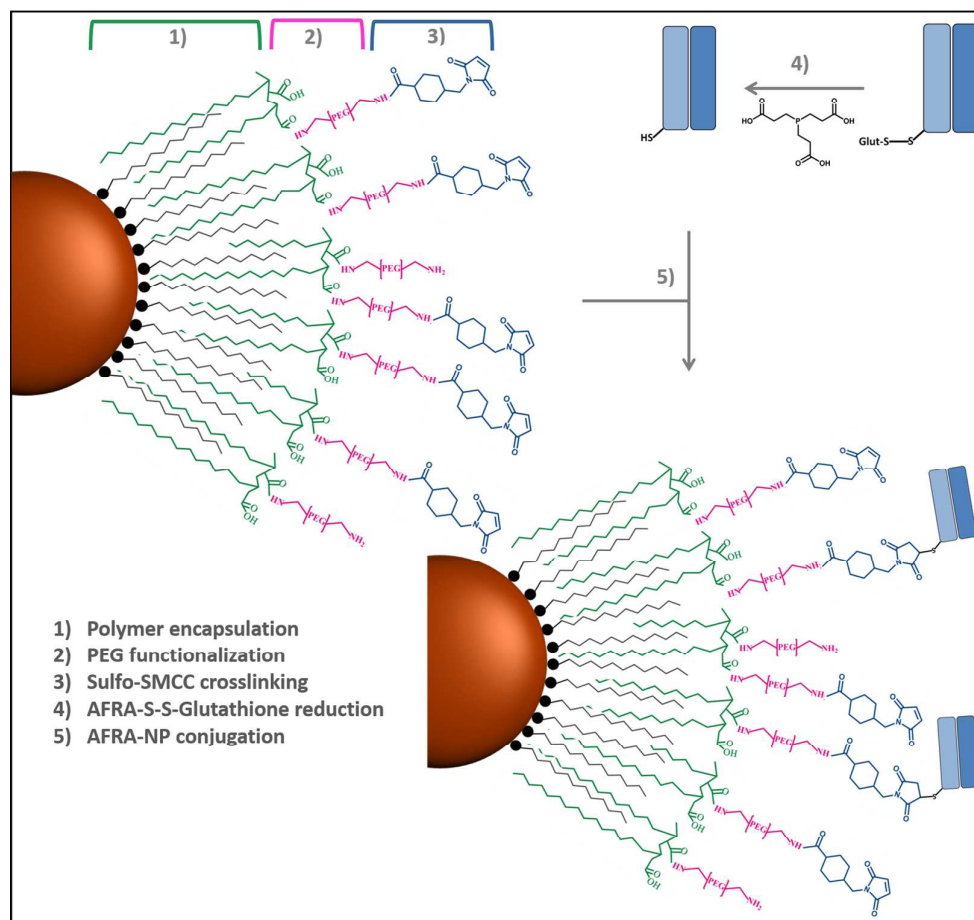


Figure 1. Sketch showing the multi-step conjugation approach used to bind the AFRA fragment to inorganic nanoparticles.

The chemical approach was implemented to allow the linkage of AFRA to different types of inorganic nanoparticles exploited for different aims in the present study.

Both fluorescent semiconductor quantum rods (QRs) and spherical magnetic iron oxide nanoparticles of two different diameters (10 and 20 nm, MNP10 and MNP20) were functionalized with AFRA. In Figure 2, the structural characterization of the NP-AFRA conjugates is reported. TEM images show the size of the inorganic core for the three distinct nanoparticles (Figures 2a, 2d and 2g). Gel electrophoresis before and after AFRA derivatization was used to demonstrate antibody conjugation to the NP (Figure 2b, 2e and 2h). Nanoparticles at the 1st (just polymer coated), 2nd (amino-PEG coated) and 5th (AFRA-functionalized) step of functionalization, as depicted in Figure 1, were loaded on the gel and at each of this step, a delay in the migration pattern was recorded. The bands corresponding to the AFRA conjugates were the most retarded due to the bigger size (Figure 2b, e and h). Coomassie staining allowed to highlight the overlapping of the protein signal with the NP band, thus confirming the presence of a covalent linkage (Figure 2 third migration lane in panels b, e and h). For QR and MNP20 the NP-AFRA bands were retained in the loading well, according to the bigger size of the complex while the 10 nm MNPs were able to

migrate even after AFRA attachment. In the case of the MNP10 and QRs, the NP-AFRA bands appear smeared with respect to the same sample PEG functionalized or polymer coated. This is likely due to the binding of a lower number of AFRA molecules per nanoparticle (a less saturated NP surface) with a bigger variability over the average size of the NP-AFRA-conjugates.

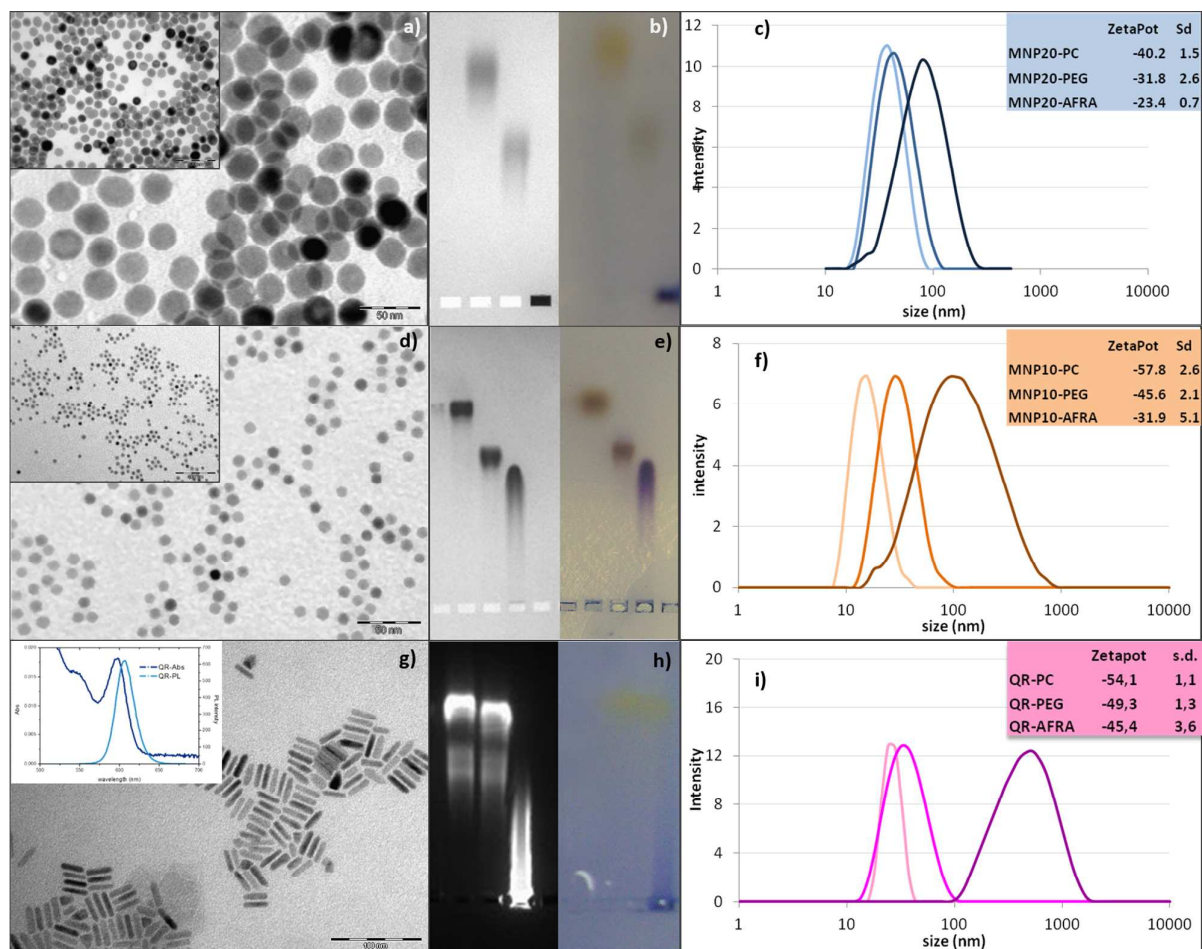


Figure 2. Characterization of the NP-AFRA conjugates by transmission electron microscopy (a, d and g), gel electrophoresis (b, e and h) and Dynamic Light Scattering measurements (c, f and i). The upper panels refer to MNP20, the central to MNP10 while the lower panel to the QR. The inset in panel g shows the absorption and fluorescent spectra of the red emitting QRs.

The amount of linked AFRA per nanoparticle was assessed by means of BCA assay. Indeed, the average number of AFRA molecules ranged from 1.6 in the case of QR to 2.8 for the MNP10 to 4.1 for the larger MNP20.

The hydrodynamic radii measured by DLS (Figure 2c, f and i) confirmed the shift of the average size peak towards higher values for each step and the broadening of the NP size when the fragment is attached. Indeed in the case of the NP-AFRA the curve is shifted at larger values and is also broadened, likely due to a poorer control over the number of AFRA fragments attached per nanoparticle (only for the 20 nm MNPs the DLS peak is less wide, thus suggesting a more saturated and compact AFRA shell).

To evaluate the capacity and the kinetic of binding of NP-AFRA to α FR, Biacore technique was used. This technique is based on Surface Plasmon Resonance for the detection of biomolecular interactions. When the binding interactions between the dextran layer functionalized with multiple folate receptors (α FR) ligands of the sensor chip and the NP-AFRA added occurs, changes in the index of refraction at the surface of the sensor chip were detected and recorded as RU (Resonance Units). The output of Biacore experiments is a sensogram, a plot of response against time, showing the progress of the interaction. The first part of the curve indicates the speed of association and the second part of the curve shows the time of analyte dissociation (NP-AFRA) from the ligand (α FR).

The sensograms (Figure 3) showed a good binding of all the NP-AFRA towards the α FR placed on the surface of a sensor-chip whereas no binding was observed with NP-PEG. These data suggest that the presence of AFRA confers to the NP the specificity for the α FR. The NPs were also tested on a lane coated with an unrelated protein and no binding was observed (data not shown). These results just underline the specificity of the interaction between the NP-AFRA on the chip which is AFRA- α FR receptor mediated.

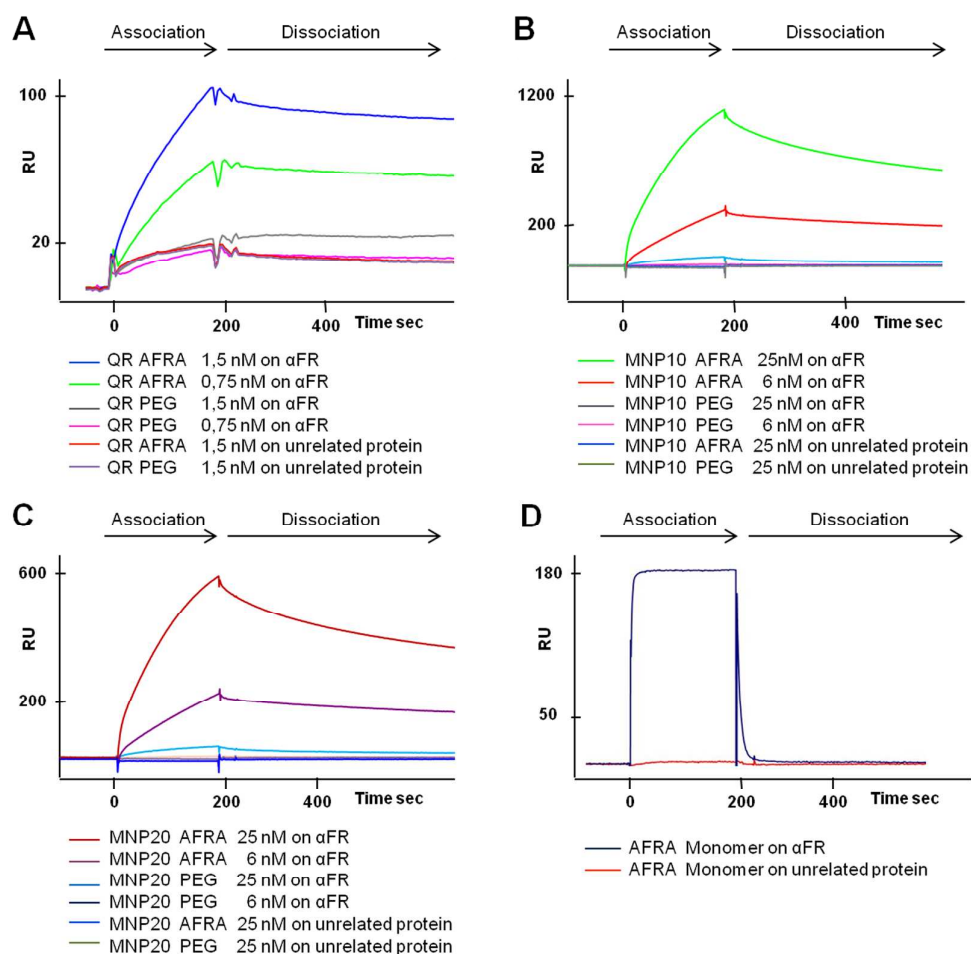


Figure 3. Biacore analysis. Sensograms illustrating the kinetic of binding of NP-AFRA and NP-PEG: QR (A), MNP10 (B) and MNP20 (C); the binding was assessed at different concentrations of analytes on a sensor-chip with immobilized recombinant α FR (target antigen). (D) Sensogram of the kinetic of binding of AFRA monomer; in this case the antibody was immobilized on the

sensorchip and the recombinant α FR was used as analyte to evaluate the kinetic of the monovalent binding. No binding of both NP-AFRA, NP-PEG and free AFRA monomer was detected on unrelated protein.

On the dissociation part of the curve for all the NP-AFRA (Figure 3 panels A, B and C), the lower slope of the NP-AFRA with respect to the non-conjugated AFRA monomer (Figure 3, panel D), indicates a stronger binding of NP-AFRA to the α FR. This in turn, suggests that more than one AFRA antibody is bound per NP; and indeed this multipoint interaction between the NP-AFRA to the α FR on the chip makes the dissociation of the AFRA functionalized nanoparticles from the α FR ligands more difficult when compared to the dissociation part of the curve of the AFRA alone (panel D of figure 3). In other words, it is much easier to wash out from the chip the AFRA alone than to remove the NP-AFRA.

These data just confirm the counting of AFRA per NP obtained from the BCA assay. In addition, the multipoint interaction of NP-AFRA allows to solve the possible problem of reduced avidity of monovalent antibody fragments with respect to the use of the whole antibody.

***In vitro* characterization of the MNP-AFRA conjugates**

Although the chemistry has been implemented with different materials, we did select the MNP for all the *in vitro* and *in vivo* study. The clear TEM contrast of MNPs allows for evaluating the binding and the intracellular pathway and localization of MNP-AFRA by TEM imaging when using IGROV1 cells over-expressing α FR (Figure 4). After 1 hour incubation, small incoming vesicles containing few nanoparticles are mainly located at the cell periphery (Figure 4a, d and e) with some of them found more in the inner part of the cytoplasm (Figure 4b and 4f). At this stage, also merging of these small vesicles clearly distinguishable (Figure 4g) into large bodies could be imaged. This might recall the folate-receptor recycling process. After 24 h, the membranes of the vesicles fused into large endosomal bodies closed to the perinuclear region (Figure 4c and Figure S1). On the contrary, for MNP-PEG after 1 hour incubation, only big endosomal bodies similar to the ones shown in Figure 4c were observed and no small vesicles were present, thus excluding the receptor-mediated endocytosis pathway (Figure S2 a-f). After 24 h incubation with both MNP-PEG and MNP-AFRA endosomes result richer in NP (Figure S1 and S2).

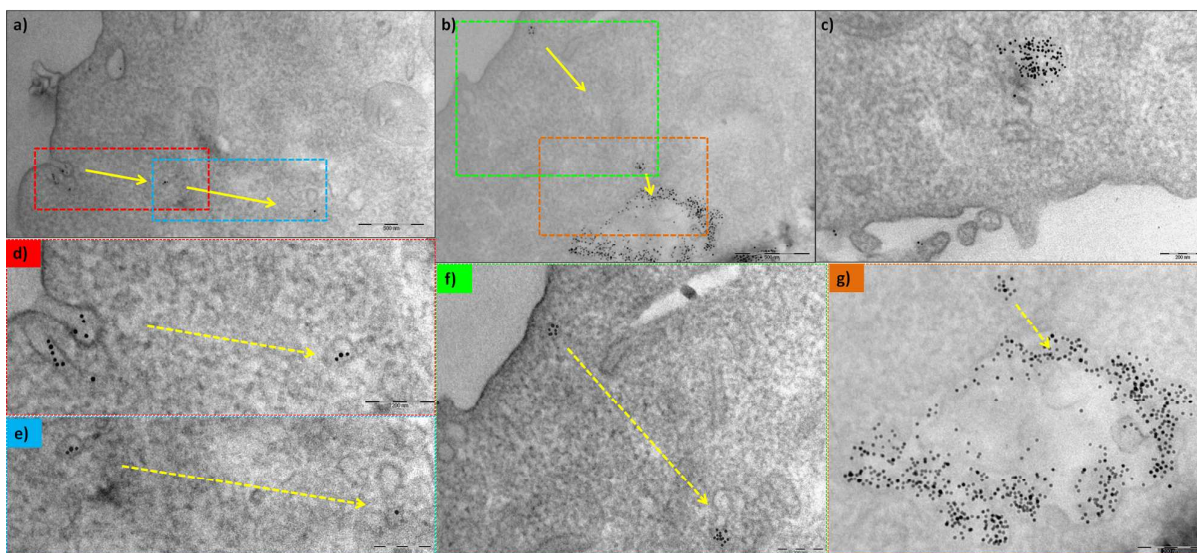


Figure 4: TEM images of IGROV cells incubated with MNP-AFRA (a-b-d-e-f-g) at 37 °C for 1h and (c)24 h. d) and e) are magnifications of dotted areas of a); while f) and g) are magnifications of dotted areas of b).

Estimation of the amount of the internalized nanoparticles was assessed via measurement of iron content by elemental analysis using ICP-AES (Inductively Coupled Plasma Atomic Emission Spectrometry), at different incubation times. The MNP internalization was facilitated by the presence of the antibody fragment, as confirmed by the higher iron content found for cells treated with the MNP-AFRA samples with respect to the MNP-PEG samples (Figure 5). Moreover, the absolute amount of iron internalized by the cell for the MNP20 is higher than that for the MNP10 regardless the administered amount. It is worth to note that in these set of experiments we have compared the MNP-AFRA to the MNP-PEG and not to the MNP-PC, because the latter are unstable in the culture media and within 1 hour they precipitate out (see Figure S3 and S4 of the ESI showing a light image of nanoparticles in the media and the hydrodynamic spectra). Indeed, on the PC-MNP, the polymer layer at the nanoparticle surface stabilize the particles only by charge and the screen effect of the charge in presence of salts and proteins favors their precipitation. On the contrary, the MNP-PEG and the MNP-AFRA samples are stable in the cell media over days as the PEG layer stabilize the nanoparticles not only by charge but also by steric hindrance. We therefore believed that it is more correct to compare the uptake on cells between equally stable nanoparticles in cell culture media rather than on PC-MNP on which the uptake on the cell is compromised by the tendency of the nanoparticles to quickly sit on top of the cells. Also, the MNP-AFRA do contain as an inner layer, the same PEG molecules of the MNP-PEG.

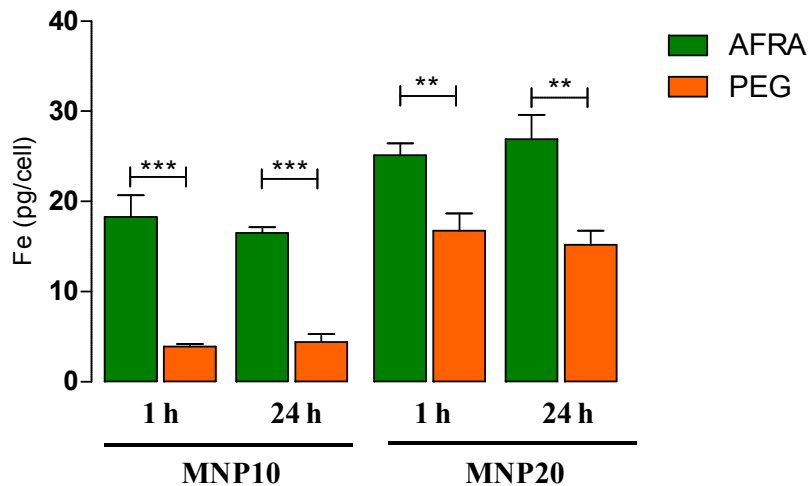


Figure 5. Assessment of the intracellular amount of Fe (pg/cell) via elemental analysis. The ovarian cancer cells IGROV1, α FR positive, were incubated 1 h in adhesion with either MNP20 or MNP10 (NP concentration 20 nM) and the amount of iron was assessed at two different time points, 1h or 24h. Cells were incubated either with MNP-AFRA or MNP-PEG. The binding of MNP10-AFRA was significantly higher than MNP10-PEG while the amount of MNP20-AFRA internalized is more than MNP10-AFRA and significant higher than MNP20-PEG, despite the binding of MNP20-PEG increased if compared with MNP10-PEG. (** $p < 0,01$ and *** $p < 0,001$, Student's *T* test)

A deeper binding *in vitro* characterization on the MNP20 was performed by FACS analysis on different cell lines (Figure 6). The adopted methodology is an indirect assay that uses a secondary fluorescent antibody against the AFRA fragment, to detect the AFRA on the MNP20-AFRA. Binding specificity of MNP20-AFRA was demonstrated on IGROV1, cells naturally expressing the α FR, and on A431FR, a cell type transfected with a vector containing the α FR gene, for inducing the α FR over-expression. On the contrary, cells transfected with the empty vector (A431MOCK) were used as negative control cell line, and did not produce any binding to MNP20-AFRA. Furthermore, MNP20-PEG did not show any binding for any of the cell lines thus confirming the NP binding specificity AFRA-mediated.

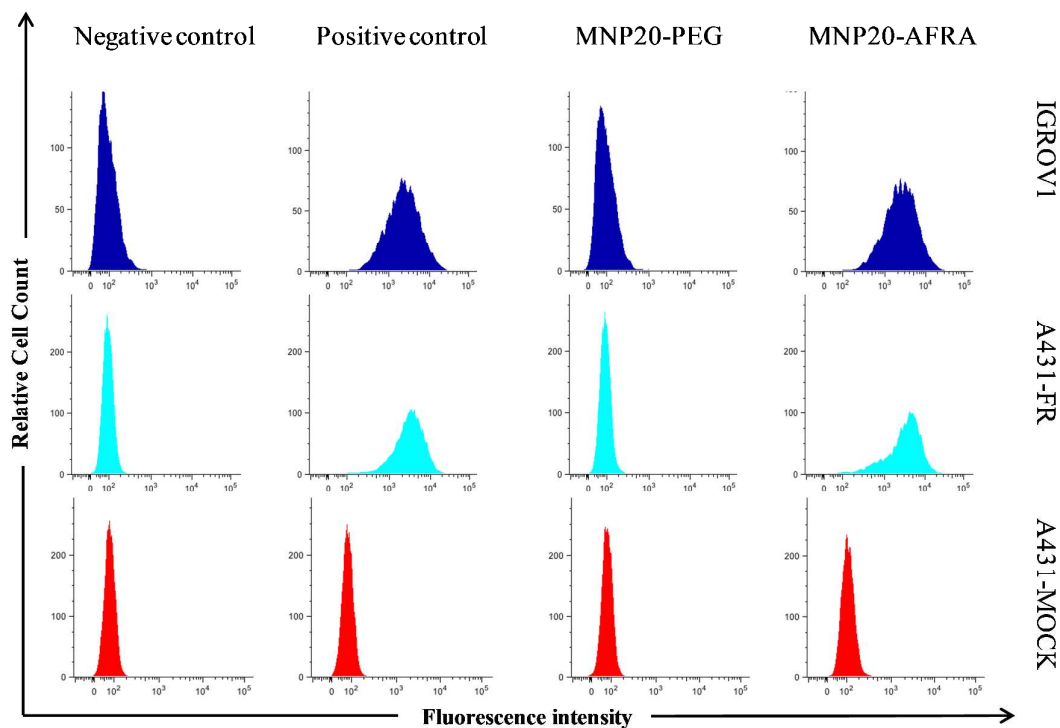


Figure 6. Flow cytometer analysis. Binding evaluation of MNP20-PEG and MNP20-AFRA on two *aFR* positive cell lines, IGROV1, A431-FR and one negative cell line A431-MOCK. MNP20-AFRA bound specifically to IGROV1 and A431-FR cells (blue and pale blue, fourth column) whereas there was no binding on A431-MOCK (red). No binding was detected for MNP20-PEG in all three cell lines (third column). AFRA purified antibody was used as positive control (second column) and for both, MNP20-AFRA and positive control (AFRA only) the binding was detected by fluorescence via an anti-human antibody Alexa488-conjugate.

It is worth to underline that elemental analysis and FACS, provide complementary information about the interactions between MNP-AFRA and the cells. Indeed FACS is aimed to study the antibody-receptor interaction at the membrane of cells in suspension (no endocytosis occurs as the measure is performed at 4°C within 1 h). The ICP instead provides a quantitative analysis of nanoparticle's accumulation, from the short to the long-term storage on cells, cultured in adherence.

The viability was evaluated by MTT assay: three incubation times (2, 4 and 24 h) and two administered NP concentrations (50 and 100 nM) were assessed for both MNP20 and MNP10 (Figure 7). The data obtained under the conditions set for this study show negligible cellular toxicity of the MNP indicating that the MNP-AFRA as well as the same MNPs coated only with PEG do not lead to any evident effect of cellular stress (Figure 7).

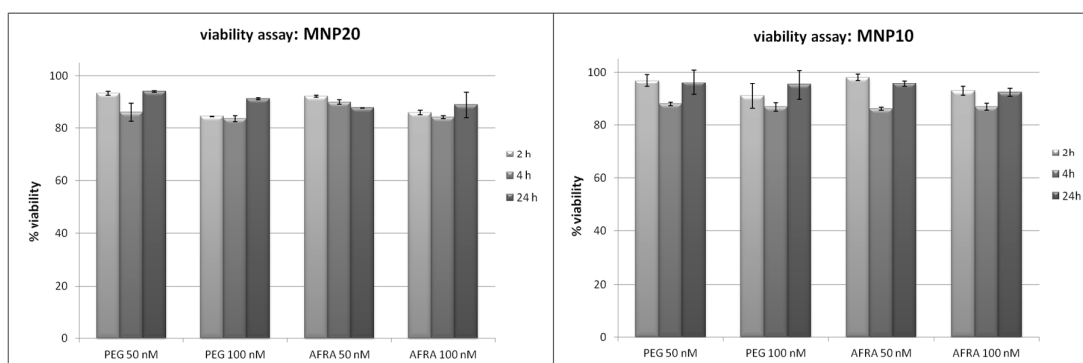


Figure 7. MTT viability assay performed with IGROV cells incubated with either MNP20 or MNP10. Cells were administered with MNP at two NP concentrations (50 and 100 nM) and for three incubation times (2, 4 and 24 h).

Once demonstrated that the methods of AFRA conjugation were broadly applicable to different types of materials, MNP20 were selected as candidates for *in vivo* targeting studies in tumor models. Indeed, the choice was made to minimize the number of animals and, at the same time, to use MNP that were within the suitable size range for therapeutic hyperthermia applications.

It has been recently reported that among different iron-based inorganic NPs, iron oxide NPs display the best heating performance in magnetic fluid hyperthermia when they have a size range around 18-20 nm, a critical size where NPs show a magnetic behavior between superparamagnetic and ferromagnetic.^{50, 51}

***In vivo* characterization of MNP20**

Tumor specific targeting of functionalized MNP after locoregional administration.

The locoregional treatment is one of current gynecological routes of administration of drugs mostly used for the chemotherapy of EOC. Based on this and with the aim to evaluate the targeting potential of MNP coupled to AFRA antibody, an intraperitoneal (IP) tumor model, mimicking the growth of the tumor in EOC patients, was initially used. The human ovarian cancer cell line OVCAR3, constitutively expressing the α FR, was grown IP for one week to allow active cell proliferation and ascites development. Tumor-bearing mice were given *via* the IP route with same doses (900 μ g of iron/animal) of either functionalized (AFRA) or control (PEG) MNP20. The mice were sacrificed at different time points, to evaluate the MNP-associated iron levels in the tumor by means of elemental analysis (Figure 8 panel A).

MNP20-AFRA from ascites significantly permeated and accumulated faster in suspension tumor cells than MNP20-PEG (Figure 8, panel B). Similarly, 3 and 6 h after MNP injection, peritoneal organs such as mesenteric tissue and genitourinary organs, typically and massively infiltrated by ovarian cancer, displayed significantly higher levels of elemental iron in tumor-bearing mice treated with MNP20-AFRA (Figure 8, Panel D). Consistently, a concomitant time-dependent reduction of MNP in the ascite fluids on animals injected with MNP20-AFRA was detected (Figure 8, Panel C), suggesting active cellular incorporation over time.

Since the intra-peritoneal injection of MNP provided nearly 100% of MNP bioavailability and given the good permeability properties of small iron nanoparticles, an increase of the signal in the peritoneal cells and organs eventually occurred also with MNP20-PEG.

Thus, regardless the nature of MNP administered to tumor-bearing mice, the amount of MNP-associated iron, quantified in the samples 24 h post MNP injection, was comparably similar between the AFRA and PEG groups, confirming that the persistence of MNP in the peritoneal cavity ultimately promoted passive penetration from the liquid phase into tumor tissue.

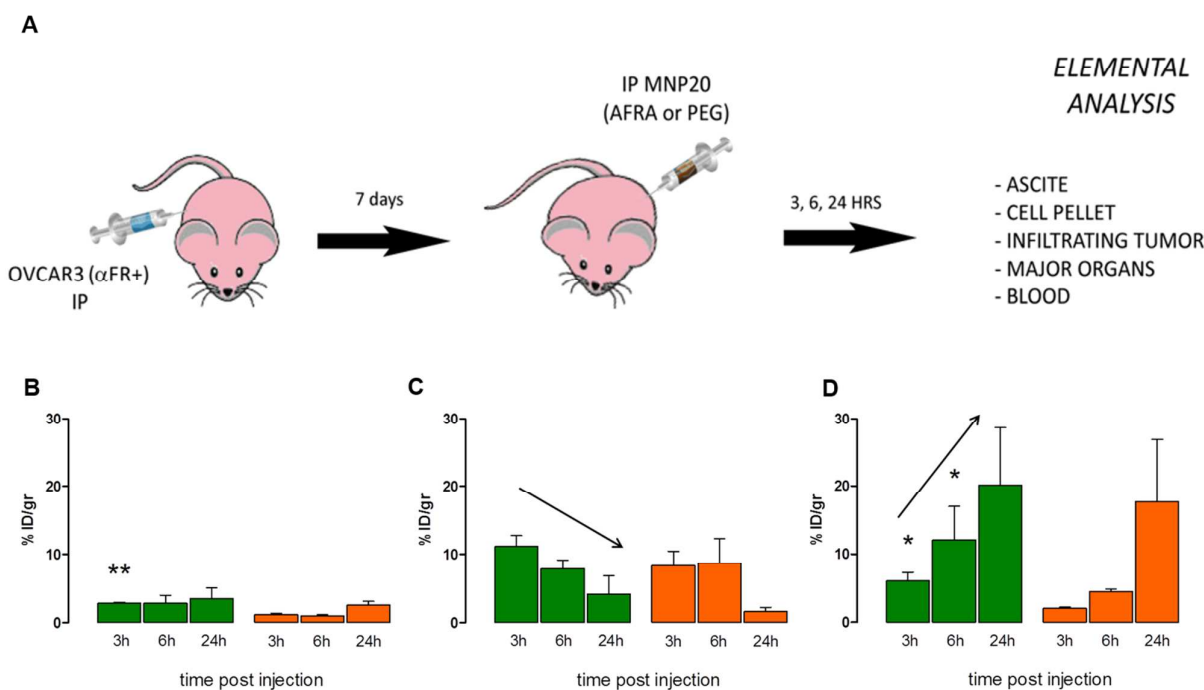


Figure 8. *In vivo* localization of MNP20 in an intraperitoneal tumor model. Scheme of treatment (A). Assessment of MNP-associated iron measured via elemental analysis over time in the cellular ascite pellet (B), ascite liquid fraction (C), and tumor-infiltrated visceral organs (mesentery and genitourinary) (D) of animals treated with MNP20-AFRA (green bars) or control MNP20-PEG (orange bars). Data are expressed as % (mean \pm SD, $n = 3-7$) of the injected dose per gram of tissue. ** $p < 0.01$ vs respective MNP20-PEG; * $p < 0.05$ vs respective MNP20-PEG, Student's *T* test.

It is important to observe, however, that the specific accumulation of the AFRA-conjugated particles in the infiltrate tumor increased to over 10% of the injected dose only 6 h post injection (Fig. 8 panel C) and the overall levels of MNP was always numerically superior when α FR targeting was present. Nevertheless, the lack of an active antigenic anchor associated to MNP20-PEG would expect to greatly reduce the intratumor persistence because of a more rapid tissue clearance. To confirm this, qualitative visualization of cell-associated MNP was carried out by electron microscopy analysis in peritoneal tumor cells. As shown in Fig. 9, clusters of MNP were clearly detectable in cells exposed to both MNP20-AFRA and MNP20-PEG. In the case of MNP20-

AFRA also small vesicles with few nanoparticles are present (Figure 9b) which is a typical feature of NP internalization by receptor-mediated endocytosis.⁵²

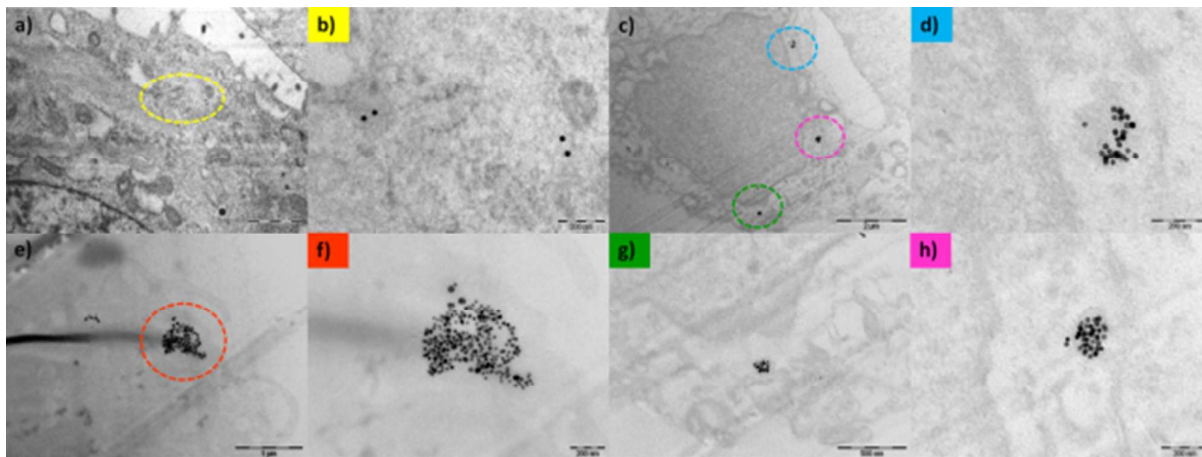


Figure 9. TEM imaging of tumor pellets grown in mice after IP injection of either MNP20-AFRA (a-b; e-f) or MNP20-PEG (c-d; g-h). Cells were harvested from the peritoneal cavity 24 h after MNP injection. The color codes for the letters correspond to the TEM magnification of the corresponding color dashed circles in the different TEM pictures.

Evaluation of distant targeting of MNP20 after systemic administration.

The capability of MNP20-AFRA to target distant tumor lesions and reach measurable accumulation was evaluated by using a tumor model able to develop subcutaneous nodules in a short time, with or without surface expression of human folate receptors. Indeed, tumor-bearing mice were injected IV with comparable amounts of MNP20-AFRA and MNP20-PEG, which were then tracked to the α FR+ and α FR- tumor nodules up to 24 h post injection (Figure 10 panel A). Quantification of elemental iron in the tumor nodules showed that MNP20-AFRA accumulated to a larger extent into α FR+ than α FR- tumors (2.8 ± 0.7 vs 1.8 ± 0.3 %ID, $p < 0.05$ unpaired t-test) 24 h post injection, while no statistical differences were detected with MNP20-PEG. Importantly, the localization of iron NP in the target α FR+ tumor significantly exceeded the value detected in the circulating plasma, suggesting a genuine and tumor specific targeting.

In addition, specific localization of AFRA functionalized NP after IV injection was further confirmed by histological analysis carried out on frozen tumor tissue slides. Tumor nodules were collected and stained with Prussian blue to detect subcellular pearls decoration. Blue iron complex staining was only demonstrated in α FR+ tumor associated to the perivascular structures (Figure 10, panel B) and significant iron accumulation was detected within the tumor stroma (Figure 10, panel C). By looking at subcellular level, localization of the iron particles appeared to be mostly perinuclear (panel C, inset). Little or no blue particles were detected in α FR- negative tumors (Figure 10, panel D).

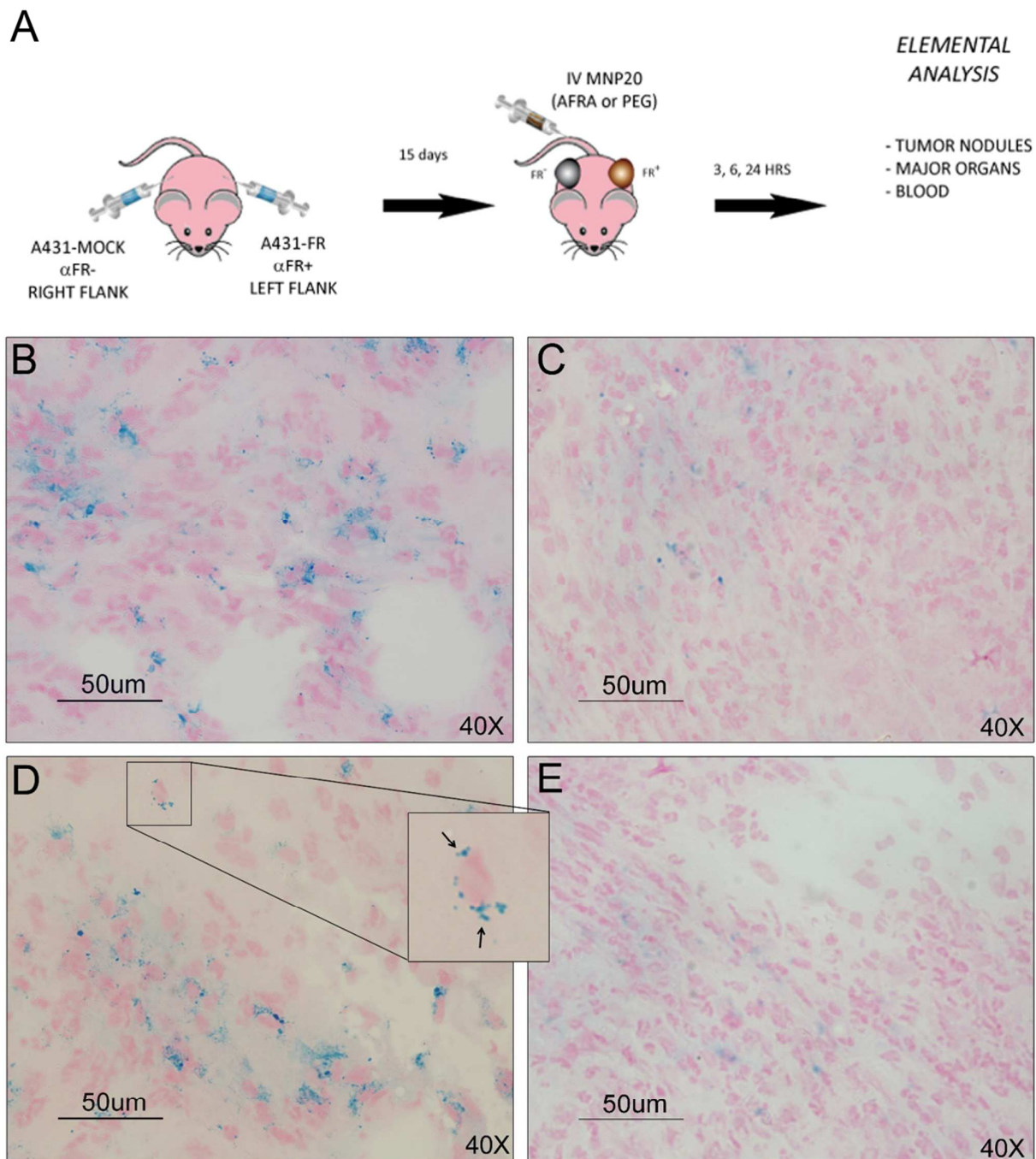


Figure 10. *In vivo* localization of MNP20 in a subcutaneous tumor model upon systemic administration. Scheme of treatment (A). Tumor nodules were collected and stained with Prussian blue to detect subcellular iron based NPs. Panels B, D: α FR positive tumors, and panel C,E: α FR negative tumor. Enlarged inset: MNP20-AFRA around the nucleus (pink stain).

Evaluation of MNP20 tumor clearing after intratumor administration.

The efficiency and the efficacy of a potential targeted MNP-driven therapy rely not only on the capability of MNP to reach the tumor lesion, but also on the ability of the NP to prevent their rapid clearance out of the tumor site. To this respect, the presence of tumor-specific antigens may greatly contribute to retain MNP within the tumor tissue. To test this, we used the subcutaneous tumor model to evaluate the persistence, over longer time points, of locally injected MNP20-AFRA or MNP20-PEG into the tumor nodule, and to study how their intratumor levels were modulated by the presence of the folate receptor. Results are shown in Figure 11.

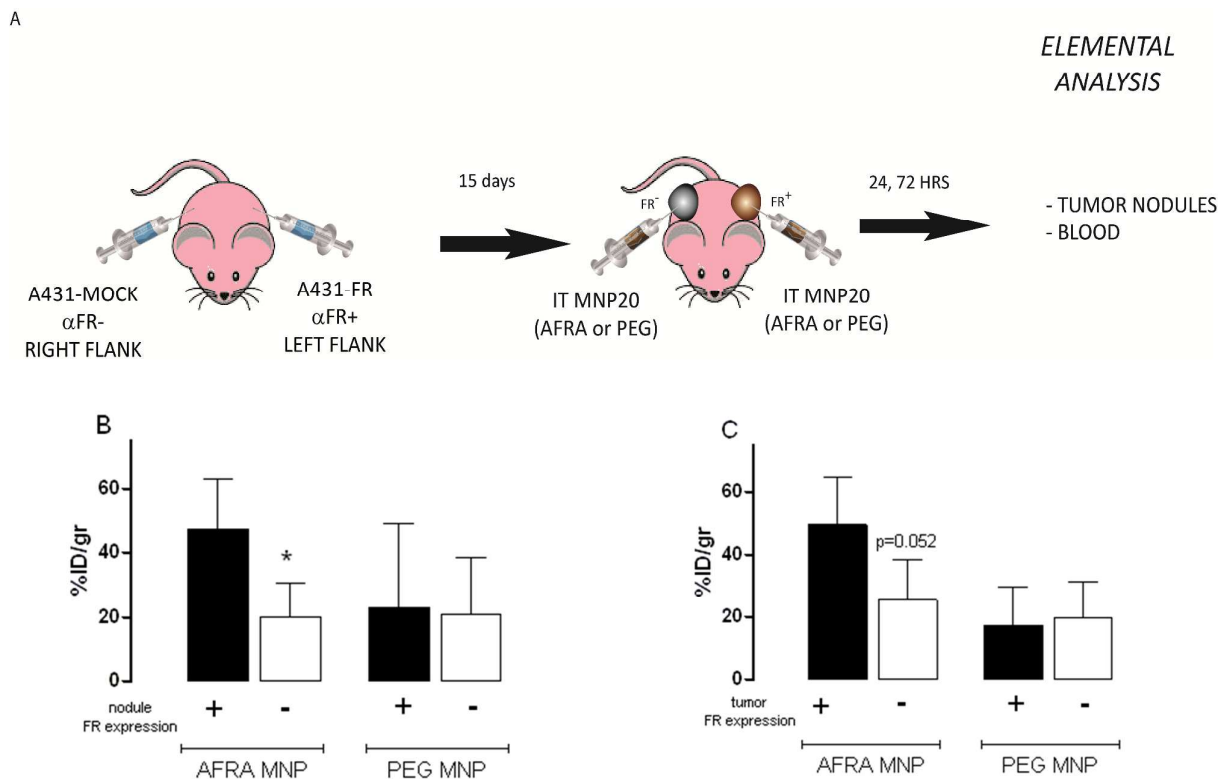


Figure 11. *In vivo* localization of MNP20 in a subcutaneous tumor model upon intratumor administration. Scheme of treatment (A). Tumor nodules were collected and assessment of MNP20-associated iron, measured via elemental analysis over time, was performed. Levels of MNP20-AFRA and MNP20-PEG measured 24 h (B) and 72 h (C) after intra-tumor injection in α FR-expressing (black bars) and α FR-negative (white bars) nodules. Data are expressed as % (mean \pm SD, $n=3-4$) of the injected dose per gram of tissue. * $p < 0.05$ vs α FR+ nodule injected with MNP20-AFRA, unpaired T test. It is shown that at 24h the difference on FR positive tumour is significant whereas at 72h a difference was still observed even if the P value (0.052) is near but nor reached the threshold selected for significance (< 0.05)

As expected, the presence of α FR allowed a higher retention levels of AFRA-functionalized MNP20, both 24 h (Fig. 11, panel B) and 72 h (Fig 11, panel C) after direct intratumor injection. Control MNP20-PEG were detected to a similar lower extent both in α FR + and α FR - nodules. Even though the local intratumor treatment does not represent a feasible clinical option in ovarian cancer, the obtained data indicated that once NPs reach the tumor, they are efficiently prevented from being cleared out only when associated to tumor-specific targeting. These data confirm the previously

anticipated hypothesis that the lack of an antigen anchor in the tumor may reduce MNP accumulation to a suboptimal extent and possibly prevent effective tumor cytotoxicity.

Evaluation of MNP20 Biodistribution

MNP20 biodistribution was determined upon systemic (IV) or loco-regional administration (IP) of either functionalized (MNP20-AFRA) or control (MNP20-PEG) nanoparticles in subcutaneous or intraperitoneal tumor-bearing mice in selected organs 3 and 24 h after injection. The MNP accumulated in the evaluated organs to a variable extent depending on the injection route, site of tumor growth and observation time.

Quantification of MNP-associated iron 3 h after administration resulted in: a significant, yet transient, iron accumulation in lungs and kidney after IV administration (MNP20-AFRA, 6.70 ± 4.77 %ID/gr) as compared to blood (1.6 ± 0 % ID/gr); a significant nonspecific accumulation in the spleen after IP injection, (% ID/gr. MNP20-AFRA: 23.1 ± 3.85 MNP20-PEG: 13.22 ± 4.34) exceeding the levels measured after IV administration by approx 15-fold. Biodistribution of MNP 24 h after IP and IV administration is shown in Figure 12. Functionalization of MNP20 with AFRA did not significantly change the bio-distribution of MNP to the major organs analyzed (fig 12A and B). No statistical difference in the biodistribution of MNP20-AFRA and MNP20-PEG was observed in mice organs after IV or IP administration. On the contrary, significant accumulation of MNP20-AFRA was noticed in α FR tumors when compared with MNP20-PEG. The most relevant observation was the 10-fold higher localization in kidneys after IP administration (Figure 12B), compared to the IV route (Figure 12A). The remarkable difference may be partly explained by the different renal function in the animals with actively-proliferating intraperitoneal tumor, which generated massive liquid exudate and putatively altered glomerular filtration but further analysis are needed to confirm this hypothesis. Furthermore, MNP independently of their functionalization, were localized preferentially into the spleen and liver. Being both liver and spleen the major organs devoted to hemocathesis and iron storage, this finding is not surprising; however, it is important to observe that persistence of high levels of MNP in the parenchyma of major organs may end up with non-obvious but significant toxicity in a long run.⁵³ It was previously demonstrated that Fe_3O_4 nanoparticles, when given systemically, may give rise to significant toxicity, in a way depending on both the size and the dose of the injected NP.⁵⁴ The amount of iron injected in the present work, should be therefore considered with a note of caution since it may cause organ toxicity in a long term by inducing parenchymal damage consequent to inflammation and oxidative stress.^{55, 56} On the other hand, this dose (between 800 or 1100 μg of iron per animal) corresponds to the dose used in an *in vivo* experiment to achieve a proof of efficacy with the most performing iron oxide nanoparticles so far available⁵⁰ and it is one of the lowest doses used in animal experiments when iron oxide is required.⁵⁷⁻⁶⁰ Noteworthy, the initial high levels in the spleen after IP administration dropped consistently at 24 h, suggesting that high and early iron accumulation might also depend on the physical interaction of MNP floating in ascitic fluid and surrounding the peritoneal organs, including aggregation behavior or electrostatic surface interaction and further observation after longer time of exposure should be tested before drawing further conclusions about toxicity.

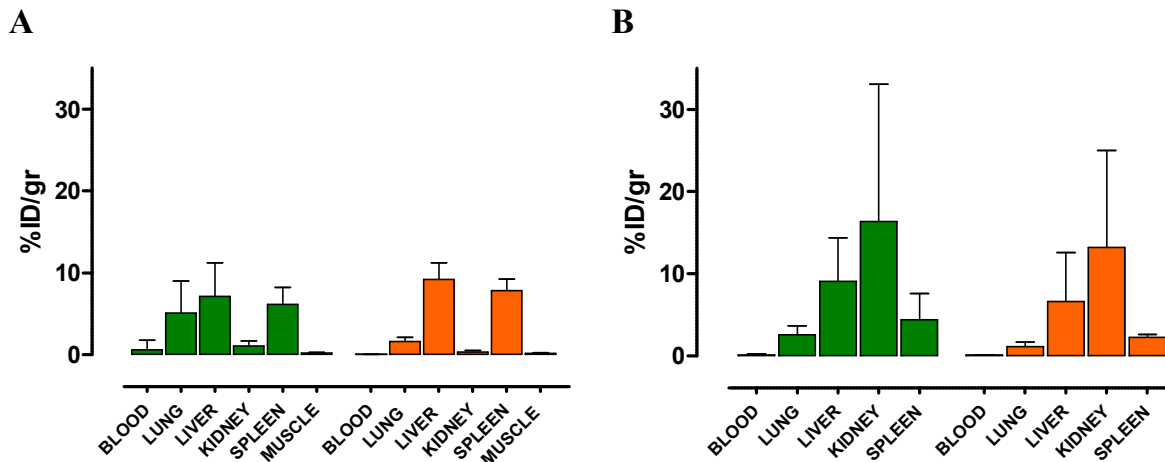


Figure 12. Biodistribution of MNP20-AFRA (green bars) or MNP20-PEG (orange bars) in selected organs of tumor bearing mice 24 h after IV (panel A) or IP (panel B) administration as assessed by elemental Fe quantification. Data are expressed as % (mean \pm SD, $n = 3-7$) of the injected dose (ID) per gram of tissue.

To the best of our knowledge only two studies of *in vivo/ex vivo* ovarian cancer targeting with MNP have been performed.^{39, 43} In these two studies cobalt ferrite NP were functionalized with a peptide that targets EphA2. In the first study, ovarian cancer cells were injected in the peritoneum of an anesthetized mouse and the nanoparticles, injected few minutes later by the same route, were able to target and to sort magnetically the floating tumor cells. In the second study the same nanoconjugate was used *ex vivo* to recognize and isolate cancer cells from ascites of ovarian cancer patients. Nevertheless, these works still leave unanswered questions about the systemic distribution and the specific accumulation of particles delivered to *in vivo* tumor growing cells.

The *in vivo* data here presented support our assumption that α FR-tumor targeting with MNP20-AFRA allows specific tumor accumulation that results as a combination of improved specificity and slower tissue wash out as compared to non-functionalized PEG-MNP. Since it is difficult to avoid non-specific accumulation of iron NP in major organs, the best approach is to develop a strategy to minimize the exposure to toxic iron levels and, at the same time, to enhance the localization to target tissues such as tumor. Unlike brain tumors, in which local administration of MNP improved chemotherapy delivery, medical treatment of ovarian cancer, which is considered a systemic disease, cannot rely on intra-tumor administration of MNP. Altogether, our data provide a proof of principle that AFRA-linked MNP may also target distant metastases of ovarian cancer cells expressing α FR on their surface and it may accumulate into the tumor stroma in a more efficient and rapid way than non-targeted MNP. The systemic or loco-regional targeting approaches may therefore represent potentially feasible ways to develop a specific and useful nanotherapy for ovarian cancer, due to the over-expression of α FR as tumor-associated marker (> 80% of clinical cases).

CONCLUSIONS

Inorganic nanoparticles can be effectively functionalized with monovalent Fab against the α FR and the magnetic nanoparticles can be quantitatively directed to bind the ovarian cancer cell surface as specific target. Further optimization of the binding chemistry is required in order to achieve reliable scale-up process.

The comparison among different *in vitro* characterization techniques has allowed to discriminate the binding features of bio-targeted nanoparticles versus PEG-coated ones. In particular, using FACS and Biacore we demonstrated that the antibody fragment (AFRA) retained its functionality and specificity towards cancer cells also after it was attached to the surface of nanoparticles. By ICP measurement we essentially confirmed that the overall content of iron in tumor cells and tissues was increased over time when MNP were functionalized with AFRA. Furthermore, MTT assay allowed to establish that these nanoparticles were non-toxic. TEM analysis on cells allows to document the cell internalization pathway of MNP-antibody fragments and the distribution into the cells seemed qualitatively different than that of MNP-PEG.

In vivo injection of a suboptimal amount of functionalized MNP demonstrated a numerical superiority in targeting α FR-expressing tumors compared to non-specific MNP. Although the MNP20-AFRA can reach the tumor site when injected systemically, accumulation in the tumor is still below the optimal level to induce a putative therapeutic effect. Indeed, better targeting is achieved by directly exposing tumor cells to MNP20-AFRA by loco-regional administration. In these contexts, tumor-specific MNP not only accumulate to a greater extent into the neoplastic lesion, to a level that can be reasonably considered appropriate for a therapeutic intervention, but also MNP20-AFRA are retained to the targeted area longer and prevented from a rapid clearing out the tumor tissue than the non-specific control.

MNP20-AFRA also build up to a significant extent in the spleen, lungs and liver. Although such accumulation is apparently transient and decreasing over time, further studies are necessary to evaluate long-term toxicity, particularly in the context of a magnetically induced therapeutic hyperthermia. A recent study suggests a metabolism degradation of iron oxide NPs over time in an *in vivo* mouse model.⁶¹

Altogether, our data provide a first proof of principle that the selective targeting of magnetic NP could represent a worthwhile effort and an added value to the goal of developing new therapeutic tools directed to the treatment of ovarian cancer through the specific targeting of tumor over-expressed α FR.

EXPERIMENTAL SECTION

Cell Lines and Antibodies. The following human tumor cell lines were used: ovarian carcinoma IGROV1 (a gift from Dr. Jean Bénard, Institute Gustave Roussy), OVCAR3 (American Type Culture Collection) and epidermoid carcinoma cells A431 (American Type Culture Collection) and A431-FR and A431-Mock transfected with α FR or empty vector respectively, isolated as previously described.⁶² All cell lines were grown in RPMI 1640 medium (Lonza), supplemented with 10% fetal calf serum (Lonza) and 2 mM glutamine (Lonza); stably transfected cells were grown with the addition of G418 at 800 μ g/mL (Gibco). AFRA⁴⁴ was used for NP conjugation and as positive control in *in vitro* NP characterization. AFRA was produced in clinical grade conditions

and verified for sterility and pyrogens below the level of detection (an automated Limulus Amoebocyte Lysate (LAL) test method was used, data not showed).

Synthesis of nanoparticles. MNP20 and MNP10 were prepared by means of thermal decomposition approach according to reported methods.^{63, 64} CdSe/CdS core/shell QRs were synthesized as described⁶⁵.

Functionalization of the nanoparticles surface with the antibody fragment. Oleic acid capped MNP and phosphonic acid capped QR were transferred into water by a polymer coating procedure developed by us and described elsewhere.⁴⁶ Then the surface of the nanoparticles was functionalized with PEG by linking amino-bearing PEG molecules to the outstretched carboxy groups of the polymer via EDC chemistry. In details in the case of MNP10 and QR the molar ratios of PEG and EDC added per NP were 1000/1 and 50000/1, respectively. In the case of MNP20 the molar ratios of PEG and EDC added per NP were 1000/1 and 100000/1, respectively, and a mixture of monoamino-PEG (MW 750 Da)/diamino-PEG (MW 2000 Da) (PEG ratio 2:1) was used. The reaction occurred in PBS pH7.4 and after 3 h stirring at RT the NP solution was washed on centrifuge filters at least 5 times.

The thiol-protected AFRA was dissolved in MES buffer (40 mM MES 10 mM EDTA pH 6.0) and reduced by Tris (2-carboxyethyl) phosphine hydrochloride (TCEP): a molar ratio TCEP/AFRA equal to 200/1 was used and the solution was kept at 4°C for 5 h on an oscillating plate. Thereafter the reduced Fab fragment was recovered on prepacked sephadex column and the concentration of the eluted protein was estimated by UV absorbance measurements at 280 nm.

Sulfosuccinimidyl-4-(*N*-maleimidomethyl)cyclohexane-1-carboxylate (Sulfo-SMCC) was used as cross-linking molecule to bind the thiol group of AFRA to the free amino moiety of diamine PEG, according to the following protocol: a solution of NP-PEG (either MNP20 or MNP10 or QR) in MES buffer was mixed with sulfo-SMCC for 40 minutes at 4 °C at a SMCC/NP molar ratio equal to 500/1. Soon after, the unbound crosslinker was removed by means of two washing steps through centrifuge filters. The collected sample was then added to the AFRA solution in MES buffer at a AFRA/NP molar ratio ranging from 40/1 in the case of MNP20, to 20/1 in the case of QR, and to 10/1 in the case of MNP10. The reaction mixture was kept under stirring over night at 4 °C. Finally, the NP were purified from the unbound AFRA by means of prepacked sephadex column (once) and by washing steps on centrifuge filters (three times).

Estimation of the NP concentration was carried out by means of elemental analysis, while the amount of AFRA molecules linked per NP was assessed by means of BCA assay. In details, a calibration curve was built up with free AFRA and then the absorbance of the AFRA conjugated to the NP was detected. Since this is a colorimetric test, after incubation with the BCA working solution, the nanoparticle samples were run on centrifuge filters and only the fractions collected under the filter were optically detected in order to remove the absorption signal of the NP. Furthermore, the absorbance value of the NP-AFRA was normalized versus the corresponding NP-PEG sample to cancel non-specific signals due to the interaction of the BCA solution with the non-protein components of the sample.

Prior to the *in vitro* and *in vivo* studies the samples, both NP-AFRA and NP-PEG, were filtered through 0.45 µm filters.

Structural and biochemical characterization. Low-Magnification TEM images were recorded on a JEOL Jem1011 microscope operating at an accelerating voltage of 100 KV. Electrophoretic characterization was carried out by running the nanoparticles through a 2% agarose gel immersed in TBE buffer (pH 8.0) for a 1 h at 100 V. After the run staining of the protein band was performed with the Coomassie solution (0.1% Coomassie Brilliant Blue R-250, 50% methanol and 10% glacial acetic acid). DLS and Zeta potential measurements were performed on a Zetasizer Nano ZS90 (Malvern, USA) equipped with a 4.0 mW He–Ne laser operating at 633 nm and with an avalanche photodiode detector. DLS measurements were performed in PBS (pH 7.4, with 137 mM NaCl, 10 mM Phosphate, 2.7 mM KCl).

The binding (or kinetic analysis) of NP was assessed first by surface plasmon resonance Biacore 2000 apparatus (Biacore AB, Uppsala, Sweden). Soluble recombinant human α FR (produced in the baculovirus expression system) was covalently bound to a CM5 sensor chip using the amine coupling kit (GE Healthcare) at an antigen concentration of 40 μ g/ml in 10 mM sodium acetate, pH 4.8. The injection of 1.0 M ethanolamine, pH 8.5 was used to block the residual activated groups. The concentration of iron was used as standard to determine the amount of NP loaded and to measure the binding, different concentration were used. NP dissociation lasted for at least 30 min and the residual NP bound to the sensor chip were detached using 100 mM glycine buffer, pH 2.7. The observations obtained were analyzed using Biaevaluation software 3.1

The binding activity and specificity of NP on α FR positive or negative live cells was evaluated by flow cytometry. Adherent cells were removed from flasks by using trypsin/EDTA and the enzyme activity blocked after cells detachment with medium containing FCS (it is well known that the expression of α FR is not modified after trypsin treatments). Cells were harvested and approximately 5×10^5 washed and incubated 1h on ice with MNP-PEG, MNP-AFRA or with AFRA Fab (10 μ g/ml) diluted in PBS and 0,03% of Bovine Serum Albumin (BSA).

Ultrastructural analysis of cells and tissues. 1×10^6 cells suspended in 5 mL of medium were seeded in a culture dish. After 24 h incubation at 37 °C the medium was replaced with fresh medium containing either MNP-AFRA or MNP-PEG at a concentration equal to 10 nM. Cells were then incubated at 37 °C for 1 or 24 h. Then, they were washed with PBS and fixed with 2.5% glutaraldehyde in 0.1 M cacodylate buffer at 4°C for 30 min. The fixed specimens were washed three times with the same buffer and 1% osmium tetroxide in cacodylate buffer was added for 1h. Thereafter, the cells were washed again and dehydrated with 25%, 50%, 75% and 100% acetone. Two steps of infiltration in a mixture of resin/acetone (1/1 and 2/1 ratios) followed and finally the specimens were embedded in 100% resin at 60 °C for 48 h. Ultrathin sections (100 nm thick) were cut on an Ultramicrotome, stained with lead citrate and observed under the electron microscope. In the case of tissue specimen times of fixation, dehydration and resin infiltration were prolonged in order to allow deeper penetration.

Quantification of NP uptake. In vitro studies: IGROV1 were seeded in each well of a 6 well-plate in 2 mL of culture medium. After 24 hours the medium was replaced with 2 mL of fresh medium containing 20 nM MNP (either MNP20 or MNP10) conjugated to AFRA or only coated with PEG. Two different time points of iron uptake were chosen. In the first cells were incubated for 1 h and iron content assessed, while in the second after 1 h of incubation the medium was replaced with fresh

one and cells were kept for additional 24 h at 37°C before iron measurement. Then the cells were washed three times with PBS and trypsinized. The cell suspension was then centrifuged, the supernatant removed and 1 mL of a concentrated HCl/HNO₃ (3/1) solution was added to digest the cells. The intracellular Fe concentration was measured by means of elemental analysis. *In vivo* studies: organs and tumors extracted from treated and control mice were quickly washed, weighted and then frozen prior to be lyophilized. Then the dry specimens were digested in concentrated HNO₃ added with 30% hydrogen peroxide. Then the samples were heated in order to allow complete dissolution of the organs. The fat component was removed by filtration prior to detect Fe amount by means of inductively coupled plasma atomic emission spectrometry (ICP-AES) and with the preparation of a Fe calibration curve. Finally, the iron amount was normalized versus the organ weight.

Viability assay. IGROV1 cells (α FR -positive cell line) and A431 (α FR -negative cell line) were grown at 37 °C and 5% CO₂ in RPMI-1640 medium supplemented with L-glutamine, penicillin, streptomycin, and 10% heat-inactivated fetal bovine serum. The viability assay (MTT test) with the 3-(4,5-dimethyl-2-thiazolyl)-2,5-diphenyl-2H-tetrazolium bromide was performed on IGROV1 cells added with MNP. 5×10^4 cells suspended in 1 mL of medium were seeded in each well of a 12 well-plate, and after 24 h incubation at 37 °C, the medium was replaced with a fresh medium containing the NP at various concentrations (50 and 100 nM) and at three time points (2, 4 and 24 h). Both MNP-PEG and MNP-AFRA for either MNP20 or MNP10 were assayed. Then the medium was removed, the cells were washed twice with phosphate buffer (pH 7.4), and 1 mL of fresh medium serum-free containing 1 mg/mL of MTT was added into each well. After 3 h of incubation at 37 °C, the dark insoluble formazan obtained was dissolved in 2 mL of DMSO, leading to a violet solution whose absorbance at 570 nm was determined. The absorbance was correlated to the percentage of vital cells, by comparing the data of the doped cells with those of the control cells.

***In vivo* injection of NP-AFRA. Tumor models**

Intraperitoneal tumor model. The ovarian cancer cell line OVCAR3 naturally expressing α FR was transplanted (20×10^6 cells) in the peritoneum of CD1 nude mice and grown for 7 days. Equivalent doses of either MNP20-AFRA or MNP20-PEG, as negative control, (16 μ moles iron, corresponding to approx. 900 μ g) were then injected IP and their accumulation in specific districts was assessed after 3, 6, and 24 hours. Relevant organs, ascites, tumor-infiltrated visceral tissues and tumor cells were collected and analyzed for iron levels by using ICP-AES.

Subcutaneous tumor model. The etherotopic model was set up by using the human cancer cell line A431, genetically modified to either express the α FR on their surface (A431-FR) or the control empty vector (A431-MOCK). Both cell lines were then injected in mice (3×10^6 cells/mouse) simultaneously in the left (A431-FR) and right flanks. After 15 days, the tumor nodules grown to a volume of approx. 6-700 mm³ and animals were given either intravenously (15-20 μ moles iron, corresponding to approx. 800-1100 μ g) or intratumor (1.5 μ moles iron, corresponding to approx. 280 μ g) with MNP20-AFRA or PEG. Relevant organs and tumor tissue were collected at different time point ranging from 3 to 72 h post MNP administration.

Perls Prussian Blue stain. Mice were euthanized by cervical dislocation and tumors were post-fixed overnight in PBS-4% paraformaldehyde solution, cryo-protected by sucrose gradient, frozen in nitrogen vapor and sectioned (6 μm thick) by using a cryostat. Sections were then stained for iron detection using Perls assay according to the manufacturer's specifications (Bio-Optica, Milano, Italy). Labeled sections were analyzed by microscopy (Nikon Eclipse TE2000-S)

ACKNOWLEDGEMENTS

We are grateful to Giammarino Pugliese for helping with sample preparation and Francesco Caroli for helping with the *in vitro* characterization. This work was supported by the European project Magnifyco (Contract NMP4-SL-2009-228622), by the Italian AIRC project (contract no. 14527 to TP) and by the EU-ITN network Mag(net)icFun (contract no. PITN-GA-2012-290248) and by the Italian FIRB projects (Nanostructured oxides, contract no.588 BAP115AYN).

REFERENCES

1. I. Mellman, G. Coukos and G. Dranoff, *Nature*, 2011, 480, 480-489.
2. K. Pliarchopoulou and D. Pectasides, *Critical Reviews in Oncology/Hematology*, 2011, 79, 17-23.
3. J. Tomasina, S. Lheureux, P. Gauduchon, S. Rault and A. Malzert-Freon, *Biomaterials*, 2013, 34, 1073-1101.
4. A. Cirstoiu-Hapca, F. Buchegger, N. Lange, L. Bossy, R. Gurny and F. Delie, *Journal of Controlled Release*, 2010, 144, 324-331.
5. M. E. Werner, S. Karve, R. Sukumar, N. D. Cummings, J. A. Copp, R. C. Chen, T. Zhang and A. Z. Wang, *Biomaterials*, 2011, 32, 8548-8554.
6. E. Vlashi, L. E. Kelderhouse, J. E. Sturgis and P. S. Low, *ACS Nano*, 2013, 7, 8573-8582.
7. E. S. Lee, Z. G. Gao, D. Kim, K. Park, I. C. Kwon and Y. H. Bae, *Journal of Controlled Release*, 2008, 129, 228-236.
8. D. Kim, Z. G. Gao, E. S. Lee and Y. H. Bae, *Molecular Pharmaceutics*, 2009, 6, 1353-1362.
9. C. L. Zavaleta, W. T. Phillips, A. Soundararajan and B. A. Goins, *International Journal of Pharmaceutics*, 2007, 337, 316-328.
10. A. Chaudhury, S. Das, R. M. Bunte and G. N. C. Chiu, *International Journal of Nanomedicine*, 2012, 7, 739-751.
11. B. Pelaz, S. Jaber, D. J. de Aberasturi, V. Wulf, T. Aida, J. M. de la Fuente, J. Feldmann, H. E. Gaub, L. Josephson, C. R. Kagan, N. A. Kotov, L. M. Liz-Marzán, H. Mattoussi, P. Mulvaney, C. B. Murray, A. L. Rogach, P. S. Weiss, I. Willner and W. J. Parak, *ACS Nano*, 2012, 6, 8468-8483.
12. O. Veiseh, J. W. Gunn and M. Zhang, *Advanced Drug Delivery Reviews*, 2010, 62, 284-304.
13. V. I. Shubayev, T. R. Pisanic and S. H. Jin, *Advanced Drug Delivery Reviews*, 2009, 61, 467-477.
14. A. Figuerola, R. Di Corato, L. Manna and T. Pellegrino, *Pharmacological Research*, 2010, 62, 126-143.
15. F. M. Kievit and M. Zhang, *Accounts of Chemical Research*, 2011, 44, 853-862.
16. L. Gu, R. H. Fang, M. J. Sailor and J.-H. Park, *ACS Nano*, 2012, 6, 4947-4954.
17. M. Levy, N. Luciani, D. Alloyeau, D. Elgrabli, V. Deveaux, C. Pechoux, S. Chat, G. Wang, N. Vats, F. Gendron, C. Factor, S. Lotersztajn, A. Luciani, C. Wilhelm and F. Gazeau, *Biomaterials*, 2011, 32, 3988-3999.
18. H. B. Na, G. Palui, J. T. Rosenberg, X. Ji, S. C. Grant and H. Mattoussi, *ACS Nano*, 2011, 6, 389-399.
19. H. B. Na, I. C. Song and T. Hyeon, *Advanced Materials*, 2009, 21, 2133-2148.

20. C. Sun, J. S. H. Lee and M. Zhang, *Advanced Drug Delivery Reviews*, 2008, 60, 1252-1265.
21. J. W. M. Bulte and D. L. Kraitchman, *Nmr in Biomedicine*, 2004, 17, 484-499.
22. S. Laurent, S. Dutz, U. O. Häfeli and M. Mahmoudi, *Advances in Colloid and Interface Science*, 2011, 166, 8-23.
23. C. S. S. R. Kumar and F. Mohammad, *Advanced Drug Delivery Reviews*, 2011, 63, 789-808.
24. K. Maier-Hauff, R. Rothe, R. Scholz, U. Gneveckow, P. Wust, B. Thiesen, A. Feussner, A. Deimling, N. Waldoefner, R. Felix and A. Jordan, *Journal of Neuro-Oncology*, 2007, 81, 53-60.
25. B. Thiesen and A. Jordan, *International Journal of Hyperthermia*, 2008, 24, 467-474.
26. A. K. Gupta and M. Gupta, *Biomaterials*, 2005, 26, 3995-4021.
27. J. E. Rosen, L. Chan, D.-B. Shieh and F. X. Gu, *Nanomedicine-Nanotechnology Biology and Medicine*, 2012, 8, 275-290.
28. A. Quarta, A. Curcio, H. Kakwere and T. Pellegrino, *Nanoscale*, 2012, 4, 3319-3334.
29. A. Vonarbourg, C. Passirani, P. Saulnier and J. P. Benoit, *Biomaterials*, 2006, 27, 4356-4373.
30. S. Laurent, D. Forge, M. Port, A. Roch, C. Robic, L. V. Elst and R. N. Muller, *Chemical Reviews*, 2008, 108, 2064-2110.
31. J. Xie, C. Xu, N. Kohler, Y. Hou and S. Sun, *Advanced Materials*, 2007, 19, 3163-+.
32. R. Bardhan, W. Chen, M. Bartels, C. Perez-Torres, M. F. Botero, R. W. McAninch, A. Contreras, R. Schiff, R. G. Pautler, N. J. Halas and A. Joshi, *Nano Letters*, 2010, 10, 4920-4928.
33. L. Fiandra, S. Mazzucchelli, C. De Palma, M. Colombo, R. Allevi, S. Sommaruga, E. Clementi, M. Bellini, D. Prospero and F. Corsi, *Acs Nano*, 2013, 7, 6092-6102.
34. C. G. Hadjipanayis, R. Machaidze, M. Kaluzova, L. Wang, A. J. Schuette, H. Chen, X. Wu and H. Mao, *Cancer Research*, 2010, 70, 6303-6312.
35. F. M. Kievit, Z. R. Stephen, O. Veiseh, H. Arami, T. Wang, V. P. Lai, J. O. Park, R. G. Ellenbogen, M. L. Disis and M. Zhang, *Acs Nano*, 2012, 6, 2591-2601.
36. L. Yang, H. Mao, Y. A. Wang, Z. Cao, X. Peng, X. Wang, H. Duan, C. Ni, Q. Yuan, G. Adams, M. Q. Smith, W. C. Wood, X. Gao and S. Nie, *Small*, 2009, 5, 235-243.
37. L. Agemy, D. Friedmann-Morvinski, V. R. Kotamraju, L. Roth, K. N. Sugahara, O. M. Girard, R. F. Mattrey, I. M. Verma and E. Ruoslahti, *Proceedings of the National Academy of Sciences of the United States of America*, 2011, 108, 17450-17455.
38. F. Corsi, L. Fiandra, C. De Palma, M. Colombo, S. Mazzucchelli, P. Verderio, R. Allevi, A. Tosoni, M. Nebuloni, E. Clementi and D. Prospero, *Acs Nano*, 2011, 5, 6383-6393.
39. K. E. Scarberry, E. B. Dickerson, J. F. McDonald and Z. J. Zhang, *Journal of the American Chemical Society*, 2008, 130, 10258-10262.
40. R. Siegel, D. Naishadham and A. Jemal, *Ca-a Cancer Journal for Clinicians*, 2012, 62, 10-29.
41. K. H. Baumann, U. Wagner and A. du Bois, *Future Oncology*, 2012, 8, 1135-1147.
42. I. Romero and R. C. Bast, *Endocrinology*, 2012, 153, 1593-1602.
43. K. E. Scarberry, E. B. Dickerson, Z. J. Zhang, B. B. Benigno and J. F. McDonald, *Nanomedicine-Nanotechnology Biology and Medicine*, 2010, 6, 399-408.
44. M. Figini, F. Martin, R. Ferri, E. Luison, E. Ripamonti, A. Zacchetti, M. Mortarino, V. D. Cioccio, G. Maurizi, M. Allegretti and S. Canevari, *Cancer Immunology Immunotherapy*, 2009, 58, 531-546.
45. T. Pellegrino, L. Manna, S. Kudera, T. Liedl, D. Koktysh, A. L. Rogach, S. Keller, J. Radler, G. Natile and W. J. Parak, *Nano Letters*, 2004, 4, 703-707.
46. R. Di Corato, A. Quarta, P. Piacenza, A. Ragusa, A. Figuerola, R. Buonsanti, R. Cingolani, L. Manna and T. Pellegrino, *Journal of Materials Chemistry*, 2008, 18, 1991-1996.
47. A. M. Smith, H. W. Duan, M. N. Rhyner, G. Ruan and S. M. Nie, *Physical Chemistry Chemical Physics*, 2006, 8, 3895-3903.
48. C. R. Sun, K. Du, C. Fang, N. Bhattarai, O. Veiseh, F. Kievit, Z. Stephen, D. H. Lee, R. G. Ellenbogen, B. Ratner and M. Q. Zhang, *Acs Nano*, 2010, 4, 2402-2410.
49. R. A. Sperling and W. J. Parak, *Philosophical Transactions of the Royal Society a-Mathematical Physical and Engineering Sciences*, 2010, 368, 1333-1383.
50. P. Guardia, R. Di Corato, L. Lartigue, C. Wilhelm, A. Espinosa, M. Garcia-Hernandez, F. Gazeau, L. Manna and T. Pellegrino, *ACS Nano*, 2012, 6, 3080-3091.
51. C. L. Dennis and R. Ivkov, *International Journal of Hyperthermia*, 2013, 29, 715-729.

52. Z. Krpetic, S. Saleemi, I. A. Prior, V. See, R. Qureshi and M. Brust, *Acs Nano*, 2011, 5, 5195-5201.
53. M. Mahmoudi, H. Hofmann, B. Rothen-Rutishauser and A. Petri-Fink, *Chemical Reviews*, 2011, 112, 2323-2338.
54. T. K. Jain, M. K. Reddy, M. A. Morales, D. L. Leslie-Pelecky and V. Labhasetwar, *Molecular Pharmaceutics*, 2008, 5, 316-327.
55. S. Sharifi, S. Behzadi, S. Laurent, M. L. Forrest, P. Stroeve and M. Mahmoudi, *Chemical Society Reviews*, 2012, 41, 2323-2343.
56. S. J. Soenen, P. Rivera-Gil, J.-M. Montenegro, W. J. Parak and S. C. De Smedt, *Nano today*, 2011, 6, 446-465.
57. A. Attaluri, R. Ma, Y. Qiu, W. Li and L. Zhu, *International Journal of Hyperthermia*, 2011, 27, 491-502.
58. S. Dutz, M. Kettering, I. Hilger, R. Müller and M. Zeisberger, *Nanotechnology*, 2011, 22, 265102.
59. E. Alphanbéry, S. Faure, O. Seksek, F. Guyot and I. Chebbi, *ACS Nano*, 2011, 5, 6279-6296.
60. D. C. R. Kolosnjaj-Tabi Jelena, Lartigue Lénaic, Marangon Iris, Guardia Pablo, Silva Amanda K. A., Luciani Nathalie, Clément Olivier, Flaud Patrice, Singh Jaykrishna V., Decuzzi Paolo, Pellegrino Teresa, Wilhelm Claire, and Gazeau Florence *Acs Nano*, 2014, Article ASAP.
61. L. Lartigue, D. Alloyeau, J. Kolosnjaj-Tabi, Y. Javed, P. Guardia, A. Riedinger, C. Péchoux, T. Pellegrino, C. Wilhelm and F. Gazeau, *ACS Nano*, 2013, 7, 3939-3952.
62. A. Coliva, A. Zacchetti, E. Luison, A. Tomassetti, I. Bongarzone, E. Seregna, E. Bombardieri, F. Martin, A. Giussani, M. Figini and S. Canevari, *Cancer Immunology Immunotherapy*, 2005, 54, 1200-1213.
63. W. W. Yu, J. C. Falkner, C. T. Yavuz and V. L. Colvin, *Chemical Communications*, 2004, 2306-2307.
64. T. Hyeon, S. S. Lee, J. Park, Y. Chung and H. Bin Na, *Journal of the American Chemical Society*, 2001, 123, 12798-12801.
65. L. Carbone, C. Nobile, M. De Giorgi, F. D. Sala, G. Morello, P. Pompa, M. Hytch, E. Snoeck, A. Fiore, I. R. Franchini, M. Nadasan, A. F. Silvestre, L. Chiodo, S. Kudera, R. Cingolani, R. Krahne and L. Manna, *Nano Letters*, 2007, 7, 2942-2950.